nature COMMUNICATIONS

ARTICLE

https://doi.org/10.1038/s41467-020-16425-z OPEN

Mott gap collapse in lightly hole-doped $Sr_{2-x}K_xIrO_4$

J. N. Nelson [1], C. T. Parzyck [1], B. D. Faeth[1], J. K. Kawasaki [1,2,3,4], D. G. Schlom [2,3] & K. M. Shen [1,3]✉

The evolution of Sr_2IrO_4 upon carrier doping has been a subject of intense interest, due to its similarities to the parent cuprates, yet the intrinsic behaviour of Sr_2IrO_4 upon hole doping remains enigmatic. Here, we synthesize and investigate hole-doped $Sr_{2-x}K_xIrO_4$ utilizing a combination of reactive oxide molecular-beam epitaxy, substitutional diffusion and in-situ angle-resolved photoemission spectroscopy. Upon hole doping, we observe the formation of a coherent, two-band Fermi surface, consisting of both hole pockets centred at (π, 0) and electron pockets centred at ($\pi/2$, $\pi/2$). In particular, the strong similarities between the Fermi surface topology and quasiparticle band structure of hole- and electron-doped Sr_2IrO_4 are striking given the different internal structure of doped electrons versus holes.

[1] Laboratory of Atomic and Solid State Physics, Department of Physics, Cornell University, Ithaca, New York 14853, USA. [2] Department of Materials Science and Engineering, Cornell University, Ithaca, New York 14853, USA. [3] Kavli Institute at Cornell for Nanoscale Science, Ithaca, New York 14853, USA. [4] Present address: Department of Materials Science and Engineering, University of Wisconsin, Madison, Wisconsin 53706, USA. ✉email: kmshen@cornell.edu

The spin–orbit-coupled Mott insulator Sr_2IrO_4 exhibits a fascinating interplay between numerous competing energy scales, including spin–orbit coupling (SOC), Coulomb repulsion (U), Hund's coupling (J_H), and has thus been subject of much recent interest[1–5]. Close similarities between Sr_2IrO_4 and the parent cuprate La_2CuO_4 have also led to theoretical proposals that hole- and electron-doped Sr_2IrO_4 could likewise exhibit unconventional superconductivity[2,6,7]. To date, the majority of work has focused on the electron-doped side of the phase diagram with reports of a momentum-dependent pseudogap in $Sr_{2-x}La_xIrO_4$[8] and a d-wave-like gap in surface K-doped Sr_2IrO_4[4,5]. These are both features associated with cuprates, although no direct signature of superconductivity has been conclusively identified. On the other hand, the behaviour of Sr_2IrO_4 upon hole doping is less clear, as the vast majority of studies have examined $Sr_2Ir_{1-x}Rh_xO_4$[9–13] and Rh substitution introduces a number of complexities beyond the doping of holes. As Rh is introduced into the IrO_2 planes, it removes a local $J_{eff} = 1/2$ moment, leading to pairs of Rh^{3+} and Ir^{5+} non-magnetic impurities[14], which is analogous to Zn or Ni substitution for Cu in cuprates[15,16]. In cuprate superconductors, the preferred doping sites are those that are not part of the CuO_2 planes, e.g., the A-site of cuprates with formula A_2CuO_4 (A = Sr or Ba). The A-sites are preferred because of the lower disorder potential that they evoke compared with sites within the CuO_2 planes; by analogy with Sr_2IrO_4, it is likely similarly advantageous to minimize disorder by doping the Sr-site with an appropriate dopant rather than to dope the Ir-site with Rh. Furthermore, Rh substitution should also change the average strength of the SOC[11], a key ingredient in the formation of the low-energy electronic structure.

To reveal the intrinsic behaviour of Sr_2IrO_4 upon hole doping, it is thus desirable to investigate a system without the intertwined complexity caused by Rh substitution. In principle, substitution of a monovalent alkali (e.g., Na^+ or K^+) on the A-site for divalent Sr^{2+} should result in hole doping without the additional complexities introduced by Rh substitution, similar to the hole doping of the cuprate $Ca_{2-x}Na_xCuO_2Cl_2$ by Na substitution[17–19]. This has been demonstrated in $A_{2-x}K_xIrO_4$ (A = Sr, Ba) to preserve the long-range magnetic order at moderate amount of doping (up to $x = 0.055$)[20–22]. At present, however, no detailed spectroscopic measurements of any kind have been reported for $A_{2-x}K_xIrO_4$ presumably due to the difficulty in synthesizing high-quality bulk single crystals. To overcome this challenge, we employ a combination of reactive oxide molecular-beam epitaxy (MBE) to synthesize initially undoped Sr_2IrO_4(001) thin films, followed by a substitutional diffusion process[23,24], which allows us to substitute K for Sr. This approach circumvents the extremely high vapour pressure of KO_2 at typical growth temperatures ($\approx 10^{-2}$ torr at 850 °C)[25], which would otherwise prevent the direct incorporation of K into the thin film; additional details about this process can be found in the Methods section. Afterwards, in-situ angle-resolved photoemission spectroscopy (ARPES) measurements of $Sr_{1.93}K_{0.07}IrO_4$ thin films allow us to disentangle, for the first time, the effects of hole doping from changes in the SOC, magnetic landscape, and strong disorder scattering in the layered iridates. In doing so, we reveal that upon hole doping, coherent quasiparticles emerge together with the collapse of the Mott gap, in contrast to what has previously been reported with Rh substitution.

Results

Chemical potential shift with doping. In principle, the addition of K into Sr_2IrO_4 can result in either hole or electron doping. If K does not replace Sr, either when adsorbed on the surface[4,5,26] or intercalated, this should result in electron doping. On the other hand, if K^+ substitutes for Sr^{2+}, this should result in hole doping. To conclusively demonstrate hole doping, we measured the shift in chemical potential $\Delta\mu$ between undoped, K surface-doped, and K-substituted samples. In Fig. 1a, we show representative energy distribution curves (EDCs) of the valence band from a single Sr_2IrO_4 sample when it is (i) initially undoped (black), (ii) following surface K-deposition (green), and finally (iii) after substitutional diffusion of K for Sr (purple). K surface deposition in step (ii) causes a shift of the spectra by $\Delta\mu = +0.5 \pm 0.1$ eV, consistent with electron doping as previously reported by Kim et al.[4,5]. In contrast, following substitutional diffusion in step (iii), all features are shifted to lower binding energy by $\Delta\mu = -0.4 \pm 0.1$ eV, in the direction consistent with hole doping as established by Louat et al.[12] via Rh substitution. This process also results in a clear change in the K 3p core levels (Fig. 1b), as K is oxidized and substituted into the SrO layer. We excluded the possibility of hole doping via Sr vacancies[27], interstitial oxygen, or oxygen vacancies[28], by verifying that the post-growth annealing steps had no observable effect when the K-deposition step was omitted (see Supplementary Note 2).

Evolution of low-energy electronic structure. To investigate the effects of K substitution, in Fig. 2 we compare an isoenergy map of an undoped Sr_2IrO_4 film at 0.3 eV binding energy (sample exhibited no weight at E_F) with a Fermi surface map of the same sample following K substitution. The isoenergy map of undoped Sr_2IrO_4 in Fig. 2a closely resembles those reported for undoped bulk crystals of Sr_2IrO_4[31]. In reality, when an electron is removed from Sr_2IrO_4 (e.g., by photoemission or hole doping) $5d^4$ holes are introduced in the IrO_2 plane, where the low-energy excitations are in fact a non-magnetic singlet $J_{eff} = 0$ and a magnetic triplet state $J_{eff} = 1$ (as described by Pärschke et al.[32]). To remain consistent with the existing iridate literature, these bands may be referred to as $J_{eff} = 1/2$ and $J_{eff} = 3/2$ bands, following the convention for the undoped $5d^5$ configuration. Furthermore, an electron addition $5d^6$ state is non-magnetic with no degrees of freedom, suggesting that electrons and holes may couple differently to the local magnetic environment. The top of the occupied $J_{eff} = 1/2$ band is at (π, 0) and (0, π), and the top of the $J_{eff} = 3/2$

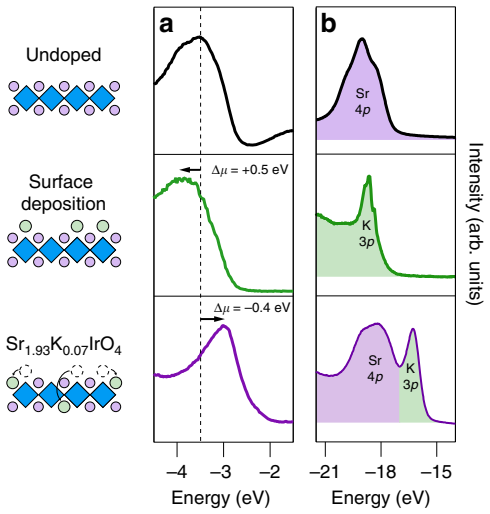

Fig. 1 Photoemission measurements showing change in chemical potential and core level spectra upon doping Sr_2IrO_4. a Measurement of the chemical potential shift, $\Delta\mu$, for a pristine undoped sample (top), after K surface deposition (middle), and after substitutional diffusion (bottom) with $h\nu = 21.2$ eV at $k_x,k_y = (0,0)$. **b** Corresponding core level spectra measured with He II photons ($h\nu = 40.8$ eV). K peak locations are consistent with reference spectra for elemental[29] and oxidized K[30].

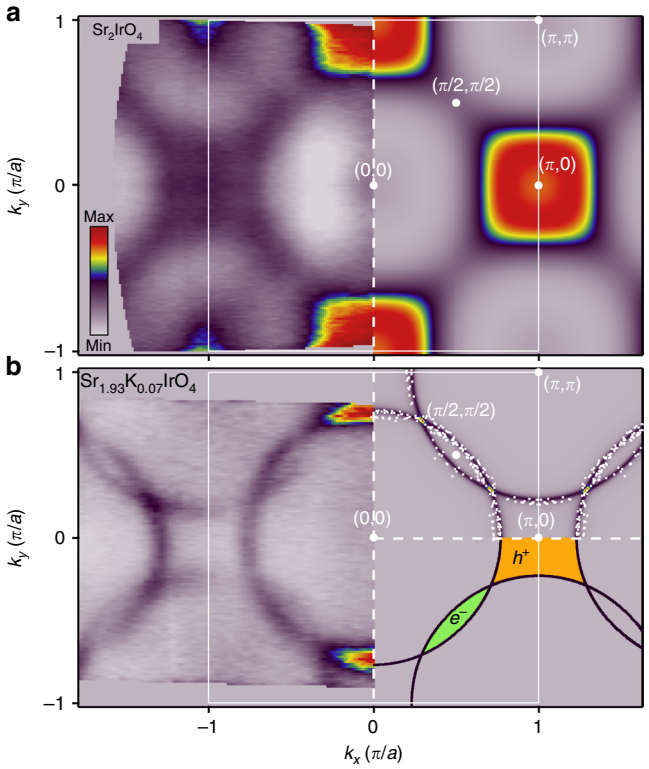

Fig. 2 Constant energy maps measured with $h\nu = 21.2$ eV and simulated using tight-binding model. a Energy isosurface at $E_B = 0.3$ eV for undoped Sr_2IrO_4 (left) together with a broadened tight binding + spin–orbit coupling + U calculation, with $U = 2$ eV (right). All data are shown in a tetragonal Brillouin zone (1 Ir per unit cell), which ignores back-folding due to the in-plane octahedral rotations, which causes a $\sqrt{2} \times \sqrt{2} R45°$ reconstruction. **b** Fermi surface of $Sr_{1.93}K_{0.07}IrO_4$ showing ARPES data (left, averaged ± 20 meV around E_F) together with a tight binding and spin–orbit coupling simulation (right) with $U = 0$ eV; hole and electron pockets are shaded orange and green, respectively. Experimentally extracted k_Fs are shown as white dots on the tight-binding model simulation.

band lies at (0,0) and (π, π), using the notation assuming an idealized, undistorted IrO_2 square lattice, as has been customary in the literature. Upon hole doping, the Fermi surface of $Sr_{2-x}K_xIrO_4$ is now clearly composed of small, elliptical electron pockets closed about (π/2, π/2) and larger square hole pockets centred around (π, 0) and (0, π). A measurement of the Luttinger volumes of these pockets indicates a hole doping of $x = 0.07 \pm 0.02$, consistent with the observed shift in chemical potential, conclusively demonstrating hole doping via K substitution.

In Fig. 3a-d, we compare spectra from undoped Sr_2IrO_4 and $Sr_{2-x}K_xIrO_4$ along both the (0,0)-(0,π) and (π/2,0)-(π/2,π) momentum cuts. For undoped Sr_2IrO_4, the broad but distinct $J_{eff} = 1/2$ band reaches its maximum at (0,-π) as reported previously in bulk single crystals, whereas for $Sr_{1.93}K_{0.07}IrO_4$ samples, this band evolves into a sharp, well-defined quasiparticle band. Comparisons of the individual EDCs at $k = (0, 1.2\pi)$ from the doped and undoped samples are shown in Fig. 3e), showing that the broad $J_{eff} = 1/2$ excitations in Sr_2IrO_4 evolve into a well-defined quasiparticle peak for $Sr_{1.93}K_{0.07}IrO_4$. In Fig. 3b, d, we compare spectra from Sr_2IrO_4 and $Sr_{1.93}K_{0.07}IrO_4$ around (π/2, π/2), which in the doped compound intersects the small, elliptical electron pockets as is clear from the momentum distribution curve (MDC) at E_F (Fig. 3d). Corresponding EDCs from Sr_2IrO_4 and $Sr_{1.93}K_{0.07}IrO_4$ taken at $k = (\pi/2, 0.6\pi)$ are shown in Fig. 3e. The lack of a large, uniform pseudogap (we observe a leading edge midpoint of less than 5 meV—see Supplementary Note 3—which is substantially less than the 30 meV shift reported in the Rh-doped samples[12,13]), and the presence of quasiparticle peaks, which are absent in $Sr_2Ir_{1-x}Rh_xO_4$, are both consistent with lower disorder scattering, in the absence of substitutional disorder directly in the IrO_2 plane.

Tight-binding model. A key distinction between $Sr_{1.93}K_{0.07}IrO_4$ and earlier studies of $Sr_2Ir_{1-x}Rh_xO_4$ is the clear presence of elliptical electron pockets, shown both in the Fermi surface map in Fig. 2b and in the band dispersion in Fig. 3d, which were not observed in $Sr_2Ir_{1-x}Rh_xO_4$. To better understand the origin of these features, we employ a tight-binding parametrization of the t_{2g} bands following refs. [8,33,34], which has previously shown good agreement with photoemission data[8]:

$$\mathcal{H} = \sum_{\langle ij\rangle\alpha\beta\sigma} t_{ij}^{\alpha\beta} c_{i\alpha\sigma}^{\dagger} c_{j\beta\sigma} + \sum_{i,\alpha=d_{xy}} \Delta_t c_{i\alpha\sigma}^{\dagger} c_{i\alpha\sigma} + \lambda \sum_i \vec{L}_i \cdot \vec{S}_i, \quad (1)$$

where $\langle ij\rangle$ are nearest-neighbour pairs of Ir sites, α and β index the t_{2g} orbitals, $t_0 = 0.35$ eV, σ indicates the spin, $\Delta t = 0.15$ eV is the tetragonal crystal field splitting and $\lambda = 0.57$ eV is the SOC parameter. These are the same values used in ref. [8]. The Coulomb repulsion U is implemented as an additional self-consistent mean-field term, which is proportional to the average electron density of each band. Additional details of the calculation can be found in Supplementary Note 4.

In Fig. 4, we show the tight-binding band structure together with extracted experimental dispersions from both Sr_2IrO_4 and $Sr_{1.93}K_{0.07}IrO_4$. We find good agreement in both the isoenergy maps (Fig. 2a) and extracted band dispersions (Fig. 4a) for the undoped case for a value of $U = 2$ eV, consistent with earlier studies of undoped Sr_2IrO_4[8]. Rigidly shifting μ into the top of the $J_{eff} = 1/2$ band of this band structure would result in a Fermi surface comprised solely of hole pockets centred at (π, 0) and (0, π), as shown in Fig. 4b. This is reminiscent of the Fermi surface of $Sr_2Ir_{1-x}Rh_xO_4$, where it was argued that the Mott gap is largely preserved up to a hole doping of $x = 0.20$[9,10,12,13], but counter to our observations in $Sr_{1.93}K_{0.07}IrO_4$.

A few important distinctions can be made between 7% hole-doped $Sr_{2-x}K_xIrO_4$ and $Sr_2Ir_{0.93}Rh_{0.07}O_4$ with a comparable hole doping from ref. [12]. First, the top of the $J_{eff} = 1/2$ band at (π,0) differs by approximately 0.1 eV (approximately +0.04 eV above E_F for Rh-doped, approximately +0.15 above E_F for K-doped). This demonstrates that $Sr_2Ir_{0.93}Rh_{0.07}O_4$ is consistent with the rigid band shift scenario in Fig. 4a. Although $Sr_2Ir_{0.93}Rh_{0.07}O_4$ only shows appreciable spectral weight near E_F around (π,0), albeit without sharp spectral features, $Sr_{1.93}K_{0.07}IrO_4$ possesses a two-sheet Fermi surface comprised of sharp, well-defined quasiparticle bands. In particular, the two-pocket fermiology observed in $Sr_{1.93}K_{0.07}IrO_4$ strongly suggests a scenario where the Mott gap has collapsed when U becomes sufficiently small (Fig. 4d-f), as the elliptical electron pocket originates from the upper Hubbard band itself. Although our data stands in clear contrast to studies of $Sr_2Ir_{1-x}Rh_xO_4$, it bears qualitative resemblance to the case of electron doping in $Sr_{2-x}La_xIrO_4$, where both hole and electron pockets have likewise been reported[8]. Nevertheless, electron vs. hole doping can be clearly distinguished from the relative sizes of the hole and electron pockets, as shown in Fig. 4e, f.

This striking similarity between electron-doped $Sr_{2-x}La_xIrO_4$ and hole-doped $Sr_{2-x}K_xIrO_4$ in the global quasiparticle band structure and Fermi surface topology, apart from a shift in the chemical potential, is unexpected given the differences in the internal structure of the doped electrons (Ir $5d^6$ in a simple $J_{eff} = 0$ state) vs. doped holes (Ir $5d^4$ with a complex spin–orbit-coupled

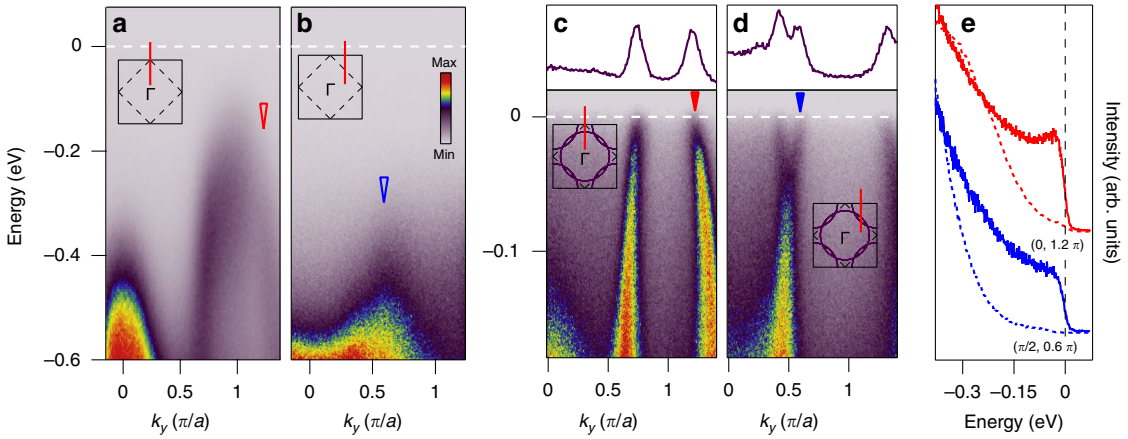

Fig. 3 Dispersions measured with $h\nu = 21.2$ eV. a ARPES spectra along (0,0)−(0, π) and **b** along (π/2,0)−(π/2,π) in undoped Sr_2IrO_4; insets show the Brillouin zone with red lines indicating the direction of the dispersion. Blue and red arrows show the momentum of the EDCs shown in **e**. **c**, **d** Corresponding ARPES spectra for $Sr_{1.93}K_{0.07}IrO_4$ intersecting the square hole pocket **c** and elliptical electron pocket **d** with MDCs at E_F shown at the top. **e** EDCs at k_F in the doped samples (solid lines) and corresponding EDCs at the same k in the undoped samples (dashed lines), indicating a clear shift of spectral weight towards the Fermi level and a quasiparticle peak at (0,1.2π/a).

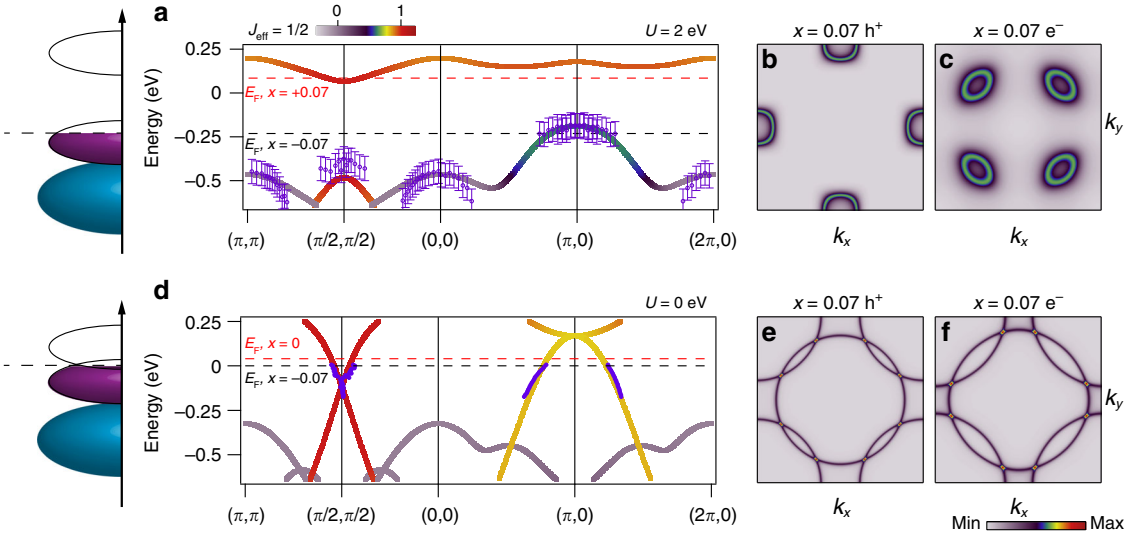

Fig. 4 Tight-binding model compared with extracted band dispersions. a Tight-binding model of the band structure with an additional mean-field Coulomb repulsion term $U = 2$ eV illustrating the behaviour of undoped Sr_2IrO_4 with extracted experimental dispersions of undoped Sr_2IrO_4 shown (purple circles), together with a schematic density of states, error bars indicated estimated uncertainty due to broad bands characteristic of insulating Sr_2IrO_4. Dashed black line indicates the chemical potential with $x = 0.07$ hole doping in a rigid band shift scenario similar to Rh-doped Sr_2IrO_4, dashed red line indicates chemical potential with $x = 0.07$ electron doping. Simulated tight-binding Fermi surfaces in a rigid band shift scenario are shown for **b** hole and **c** electron doping. **d** Tight-binding model with $U = 0$ eV, where the Mott gap has collapsed with extracted experimental dispersions of $Sr_{1.93}K_{0.07}IrO_4$ (purple circles) together with a schematic density of states. Simulated tight-binding Fermi surfaces when $U = 0$ eV shown for hole **e** and electron doping **f**.

multiplet structure). This surprising apparent symmetry between electron and hole doping should motivate future many-body calculations (e.g., Hubbard, t–J model, or dynamical mean-field theory calculations), which explicitly consider the complex multiplet structure of hole-doped Sr_2IrO_4.

Despite the apparent symmetry of the global electronic structure upon both electron and hole doping, there remain important distinctions between the two systems at the lowest energy scales. Whereas the electron-doped iridates (surface K or La substitution) in a similar doping range exhibit a large (20 meV), d-wave-like pseudogap at E_F, we do not experimentally resolve a pseudogap to within 5 meV.

Discussion

The differences between $Sr_{2-x}K_xIrO_4$ and $Sr_2Ir_{1-x}Rh_xO_4$ allow us to elucidate the intrinsic effects of hole doping vs. the additional effects caused by Rh substitution. The lack of electron pockets in the Rh-doped materials is suggestive of a rigid band shift scenario where the Mott gap is largely preserved, in contrast to $Sr_{2-x}K_xIrO_4$, where we find that the Mott gap collapses and coherent quasiparticle excitations are formed. A possible explanation is that structural and magnetic disorder in the IrO_2 planes may cause holes to be strongly localized around Rh dopants, inhibiting free carriers from effectively screening the Mott gap, whereas for the K-doped materials, the carriers are

more delocalized and are thereby able to more efficiently screen the strong Coulomb interactions. In addition, the existence of coherent quasiparticle peaks and the lack of a large pseudogap in $Sr_{2-x}K_xIrO_4$ also suggests that the incoherent metallic and the large pseudogap reported in $Sr_2Ir_{1-x}Rh_xO_4$ are likely induced by substitutional disorder in the IrO_2 plane[12], rather than an intrinsic property of hole-doped iridates.

Our findings point towards a universal underlying electronic structure upon doping Sr_2IrO_4, irrespective of the sign of the carriers, and thus a more symmetric doping phase diagram than previously realized. This stands in contrast to the cuprates, which exhibit a fundamental asymmetry between electron and hole doping[35]. Whereas the evolution of the Fermi surface contours in electron-doped cuprates can be qualitatively modelled by introducing a (π, π) spin–density wave via a conventional weak coupling phenomenology[36], explaining the disconnected Fermi arcs of the hole-doped cuprates remains an outstanding challenge for sophisticated many-body approaches, which necessarily include strong local interactions[37]. Furthermore, the Mott gap in the cuprates appears far more robust upon doping, where spectral weight is gradually transferred from the Hubbard to low-energy quasiparticle bands[38,39], whereas the gap in both hole- and electron-doped iridates appears to collapse far more rapidly. These differences may arise from the fundamentally weaker on-site Coulomb repulsion in the Ir 5*d* orbitals vs. the Cu 3*d* orbitals. Another distinction is that the cuprates are charge-transfer insulators where the hole- and electron-doped states have stronger O 2*p* vs. Cu 3*d* character, respectively, whereas the iridates are better described as Mott insulators where both the hole- and electron-doped states are of primarily Ir 5*d* orbital character, although they have very different internal magnetic structure[32]. Future work including detailed doping dependence of the electronic structure and magnetism, and a study of the electronic structure with advanced many-body techniques such as dynamical mean-field theory used in electron-doped Sr_2IrO_4[40,41], will be necessary to fully explain the collapse of the Mott gap in hole-doped $Sr_{2-x}K_xIrO_4$ and the symmetric, universal electronic structure upon both hole and electron doping.

Methods

Film growth. Epitaxial Sr_2IrO_4(001) thin films were grown on single-crystalline $(LaAlO_3)_{0.3}$ $(SrAl_{1/2}Ta_{1/2}O_3)_{0.7}$ substrates by MBE at a substrate temperature of 850 °C as measured by an optical pyrometer with a measurement wavelength of 980 nm, in a background partial pressure of 1×10^{-6} torr of distilled ozone (80% O_3 + 20% O_2). A 7 nm buffer layer of $SrIrO_3$ was initially deposited, followed by 20 nm of Sr_2IrO_4; the conducting $SrIrO_3$ layer facilitated measurements below 100 K. Additional details about the growth may be found in refs. [42,43] and in Supplementary Note 1.

Substitutional diffusion. K substitution was achieved through a substitutional diffusion process[23,24] where K was deposited on an undoped Sr_2IrO_4 film using a SAES evaporator at temperatures below 70 K and then annealed at a temperature of 300 °C in vacuum, followed by exposure to 1×10^{-6} torr of ozone at 300 °C for 20 min (both 10% and 80% O_3 were used). Multiple doped samples synthesized and investigated in this study showed highly consistent values in the chemical potential shift, near-E_F electronic structure, and extracted hole concentrations, despite significant variations in the amounts of K deposited, annealing times, or ozone concentration. This method was used because of the extremely high vapour pressure of KO_2 ($\approx 1 \times 10^{-2}$ torr at 850 °C), which prevents the direct incorporation of K into a $Sr_{2-x}K_xIrO_4$ film at its growth temperature of 850 °C.

ARPES measurements. Following growth, the samples were transferred for ARPES measurements using He Iα ($h\nu = 21.2$ eV) photons with an energy resolution of $\Delta E = 11$ meV at a temperature of 15 K. All stages described occurred within a single ultrahigh vacuum manifold, i.e., the samples were never exposed to air.

Data availability

The data that support the findings of this study are available from the corresponding author upon reasonable request.

Received: 19 October 2019; Accepted: 23 April 2020;
Published online: 22 May 2020

References

1. Jackeli, G. & Khaliullin, G. Mott insulators in the strong spin-orbit coupling limit: From Heisenberg to a quantum compass and Kitaev models. *Phys. Rev. Lett.* **102**, 017205 (2009).
2. Wang, F. & Senthil, T. Twisted hubbard model for Sr_2IrO_4: magnetism and possible high temperature superconductivity. *Phys. Rev. Lett.* **106**, 136402 (2011).
3. Rau, J. G., Lee, E. K.-H. & Kee, H.-Y. Spin-orbit physics giving rise to novel phases in correlated systems: iridates and related materials. *Annu. Rev. Condens. Matter Phys.* **7**, 195–221 (2016).
4. Kim, Y. K. et al. Fermi arcs in a doped pseudospin-1/2 Heisenberg antiferromagnet. *Science* **345**, 187–190 (2014).
5. Kim, Y. K., Sung, N. H., Denlinger, J. D. & Kim B. J. Observation of a d-wave gap in electron doped Sr_2IrO_4. *Nat. Phys.* **12**, 1–6 (2015).
6. Watanabe, H., Shirakawa, T. & Yunoki, S. Monte Carlo study of an unconventional superconducting phase in iridium oxide $J_{eff} = 1/2$ mott insulators induced by carrier doping. *Phys. Rev. Lett.* **110**, 027002 (2013).
7. Meng, Z. Y., Kim, Y. B. & Kee, H.-Y. Odd-parity triplet superconducting phase in multiorbital materials with a strong spin-orbit coupling: application to doped Sr_2IrO_4. *Phys. Rev. Lett.* **113**, 177003 (2014).
8. De La Torre, A. et al. Collapse of the mott gap and emergence of a nodal liquid in lightly doped Sr_2IrO_4. *Phys. Rev. Lett.* **115**, 176402 (2015).
9. Cao, Y. et al. Hallmarks of the Mott-metal crossover in the hole-doped pseudospin-1/2 Mott insulator Sr_2IrO_4. *Nat. Commun.* **7**, 11367 (2016).
10. Brouet, V. et al. Transfer of spectral weight across the gap of Sr_2IrO_4 induced by La doping. *Phys. Rev. B* **92**, 081117 (2015).
11. Zwartsenberg, B. et al. Spin-orbit-controlled metal-insulator transition in Sr_2IrO_4. *Nat. Phys.* **16**, 290–294 (2020).
12. Louat, A. et al. Formation of an incoherent metallic state in Rh-doped Sr_2IrO_4. *Phys. Rev. B* **97**, 161109 (2018).
13. Louat, A. et al. ARPES study of orbital character, symmetry breaking, and pseudogaps in doped and pure Sr_2IrO_4. *Phys. Rev. B* **100**, 205135 (2019).
14. Clancy, J. P. et al. Dilute magnetism and spin-orbital percolation effects in $Sr_2Ir_{1-x}Rh_xO_4$. *Phys. Rev. B* **89**, 054409 (2014).
15. Keimer, B. et al. Néel transition and sublattice magnetization of pure and doped La_2CuO_4. *Phys. Rev. B* **45**, 7430–7435 (1992).
16. Fujishita, H. & Sato, M. Comparison of the normal state properties between the superconducting and the nonsuperconducting metallic phases in $La_{2-y}Sr_yCu_{-x}Ni_xO_4$. *Solid State Commun.* **72**, 529–535 (1989).
17. Kohsaka, Y. et al. Growth of Na-doped $Ca_2CuO_2Cl_2$ single crystals under high pressures of several Gpa. *J. Am. Chem. Soc.* **124**, 12275–12278 (2002).
18. Hanaguri, T. et al. A 'checkerboard' electronic crystal state in lightly hole-doped $Ca_{2-x}Na_xCuO_2Cl_2$. *Nature* **430**, 1001–1005 (2004).
19. Shen, K. M. et al. Nodal quasiparticles and antinodal charge ordering in $Ca_{2-x}Na_x$ CuO_2Cl_2. *Science* **307**, 901–904 (2005).
20. Okabe, H., Isobe, M., Takayama-Muromachi, E., Takeshita, N. & Akimitsu, J. Carrier doping effect for transport properties of a spin-orbit Mott insulator Ba_2IrO_4. *Phys. Rev. B* **88**, 075137 (2013).
21. Ge, M. et al. Lattice-driven magnetoresistivity and metal-insulator transition in single-layered iridates. *Phys. Rev. B* **84**, 100402 (2011).
22. Terashima, K. et al. Determination of the local structure of $Sr_{2-x}M_xIrO_4$ (M = K, La) as a function of doping and temperature. *Phys. Chem. Chem. Phys.* **20**, 23783–23788 (2018).
23. Shaw, D. in *Springer Handbook of Electronic and Photonic Materials* 133–149 (Springer International Publishing, 2017).
24. Koumetz, S. et al. Post-growth diffusion of Be doped InGaAs epitaxial layers: experimental and simulated distributions. *Mater. Sci. Eng. B* **37**, 208–211 (1996).
25. Lamoreaux, R. H. & Hildenbrand, D. L. High temperature vaporization behavior of oxides. i. alkali metal binary oxides. *J. Phys. Chem. Ref. Data* **13**, 151–173 (1984).
26. Yan, Y. J. et al. Electron-doped Sr_2IrO_4: an analogue of hole-doped cuprate superconductors demonstrated by scanning tunneling microscopy. *Phys. Rev. X* **5**, 041018 (2015).
27. Kong, J. et al. Crystal structure and physical properties of the Sr-vacant spin-orbit-coupling induced Mott insulator $Sr_{2-x}IrO_4$. *Solid State Commun.* **220**, 39–44 (2015).
28. Korneta, O. B. et al. Electron-doped $Sr_2IrO_{4-\delta}(0 \le \delta \le 0.04)$: Evolution of a disordered $J_{eff} = \frac{1}{2}$ Mott insulator into an exotic metallic state. *Phys. Rev. B* **82**, 115117 (2010).
29. Wertheim, G. K. & Riffe, D. M. Evidence for crystal-field splitting in surface-atom photoemission from potassium. *Phys. Rev. B* **52**, 14906–14910 (1995).

30. Mansour, A. N. & Melendres, C. A. Characterization of $KNiIO_6$ by XPS. *Surf. Sci. Spectra* **3**, 287–295 (1994).
31. Kim, B. J. et al. Novel $J_{eff} = 1/2$ Mott state induced by relativistic spin-orbit coupling in Sr_2IrO_4. *Phys. Rev. Lett.* **101**, 076402 (2008).
32. Pärschke, E. M., Wohlfeld, K., Foyevtsova, K. & van den Brink, J. Correlation induced electron-hole asymmetry in quasi- two-dimensional iridates. *Nat. Commun.* **8**, 686 (2017).
33. Carter, J.-M., Shankar, V. V. & Kee, H.-Y. Theory of metal-insulator transition in the family of perovskite iridium oxides. *Phys. Rev. B* **88**, 035111 (2013).
34. Jin, H., Jeong, H., Ozaki, T. & Yu, J. Anisotropic exchange interactions of spin-orbit-integrated states in Sr_2IrO_4. *Phys. Rev. B* **80**, 075112 (2009).
35. Armitage, N. P., Fournier, P. & Greene, R. L. Progress and perspectives on electron-doped cuprates. *Rev. Mod. Phys.* **82**, 2421–2487 (2010).
36. Armitage, N. P. et al. Anomalous electronic structure and pseudogap effects in $Nd_{1.85}Ce_{0.15}CuO_4$. *Phys. Rev. Lett.* **87**, 147003 (2001).
37. Damascelli, A., Hussain, Z. & Shen, Z.-X. Angle-resolved photoemission studies of the cuprate superconductors. *Rev. Mod. Phys.* **75**, 473–541 (2003).
38. Armitage, N. P. et al. Doping dependence of an *n*-type cuprate superconductor investigated by angle-resolved photoemission spectroscopy. *Phys. Rev. Lett.* **88**, 257001 (2002).
39. Shen, K. M. et al. Missing quasiparticles and the chemical potential puzzle in the doping evolution of the cuprate superconductors. *Phys. Rev. Lett.* **93**, 267002 (2004).
40. Martins, C. et al. Nonlocal Coulomb correlations in pure and electron-doped Sr_2IrO_4: spectral functions, Fermi surface, and pseudo-gap-like spectral weight distributions from oriented cluster dynamical mean-field theory. *Phys. Rev. Mater.* **2**, 032001 (2018).
41. Moutenet, A., Georges, A. & Ferrero, M. Pseudogap and electronic structure of electron-doped Sr_2IrO_4. *Phys. Rev. B* **97**, 155109 (2018).
42. Nie, Y. F. et al. Interplay of spin-orbit interactions, dimensionality, and octahedral rotations in semimetallic $SrIrO_3$. *Phys. Rev. Lett.* **114**, 016401 (2015).
43. Kawasaki, J. K., Uchida, M., Paik, H., Schlom, D. G. & Shen, K. M. Evolution of electronic correlations across the rutile, perovskite, and Ruddelsden-Popper iridates with octahedral connectivity. *Phys. Rev. B* **94**, 121104 (2016).

Acknowledgements

This work was supported through the National Science Foundation [Platform for the Accelerated Realization, Analysis, and Discovery of Interface Materials (PARADIM)] under Cooperative Agreement Number DMR-1539918, NSF DMR-1709255, and the Air Force Office of Scientific Research Grant Number FA9550-15-1-0474. This research is funded in part by the Gordon and Betty Moore Foundation's EPiQS Initiative through Grant Number GBMF3850 to Cornell University. J.N.N. and B.D.F. acknowledge support from the NSF Graduate Research Fellowship under Grant Number DGE-1650441. C.T.P. acknowledges support from the Center for Bright Beams, NSF award PHY-1549132. Substrate preparation was performed in part at the Cornell NanoScale Facility, a member of the National Nanotechnology Coordinated Infrastructure (NNCI), which is supported by the NSF (Grant Number ECCS-1542081). This work made use of the Cornell Center for Materials Research Shared Facilities, which are supported through the NSF MRSEC programme (DMR-1719875).

Author contributions

J.N.N. performed the ARPES measurements and synthesized the thin films, with assistance from C.T.P., B.D.F., and J.K.K., and guidance from D.G.S. and K.M.S. J.N.N. performed the tight-binding calculations. J.N.N. and K.M.S. conceived the project and wrote the manuscript with contributions from all authors. K.M.S. supervised the project.

Competing interests

The authors declare no competing interests.

Additional information

Supplementary information is available for this paper at https://doi.org/10.1038/s41467-020-16425-z.

Correspondence and requests for materials should be addressed to K.M.S.

Peer review information *Nature Communications* thanks the anonymous reviewer(s) for their contribution to the peer review of this work. Peer reviewer reports are available.

Reprints and permission information is available at http://www.nature.com/reprints

Publisher's note Springer Nature remains neutral with regard to jurisdictional claims in published maps and institutional affiliations.

Supplementary Information: Mott gap collapse in lightly hole-doped $Sr_{2-x}K_xIrO_4$

J. N. Nelson,[1] C. T. Parzyck,[1] B. D. Faeth,[1] J.K. Kawasaki,[1,2,3,4] D. G. Schlom,[2,3] and K. M. Shen[1,3,*]

[1]*Laboratory of Atomic and Solid State Physics, Department of Physics, Cornell University, Ithaca, New York 14853, USA*

[2]*Department of Materials Science and Engineering, Cornell University, Ithaca, New York 14853, USA*

[3]*Kavli Institute at Cornell for Nanoscale Science, Ithaca, New York 14853, USA*

[4]*Current Address: Department of Materials Science and Engineering, University of Wisconsin, Madison, Wisconsin 53706, USA*

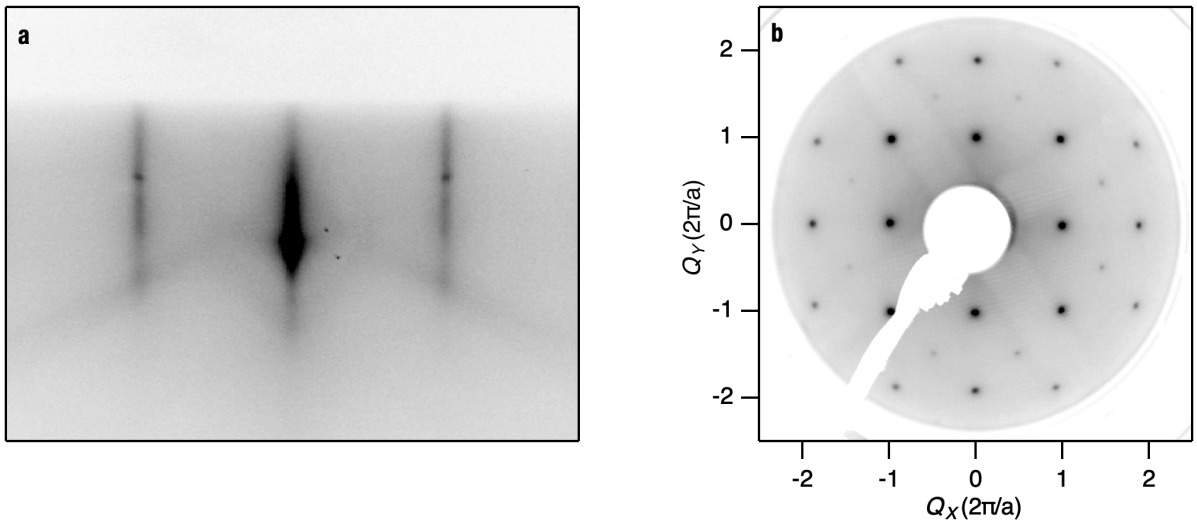

Supplementary Figure 1. Electron diffraction measurements of $Sr_{1.93}K_{0.07}IrO_4$. **a** RHEED image along the [110] azimuth showing sharp streaks indicating smooth film growth. **b** 200 eV LEED image showing a well ordered surface with half order spots indicating a $\sqrt{2} \times \sqrt{2}R45°$ reconstruction.

Supplementary Note 1: Film Growth and Characterization

Thin films of Sr_2IrO_4 were grown on a grounding layer of $SrIrO_3$ on (001)-oriented single-crystal $(LaAlO_3)_{0.3}$ $(SrAl_{1/2}Ta_{1/2}O_3)_{0.7}$ (LSAT) substrates by reactive oxide molecular-beam epitaxy (MBE) in a dual-chamber Veeco GEN10 system. A background partial pressure of 1×10^{-6} torr of distilled ozone (80% O_3 + 20% O_2) was used and the substrate temperature (as measured by an optical pyrometer with a measurement wavelength of 980 nm) was 850 °C for the Sr_2IrO_4 growth and 640 °C for the $SrIrO_3$ growth. A Sr flux of 1×10^{13} atoms $cm^{-2}s^{-1}$ was evaporated from a low temperature effusion cell, and Ir was supplied by a electron beam evaporator. Ir and Sr were codeposited during the growth with the non stoichiometric flux ratio of Sr/Ir = 1.15 for the Sr_2IrO_4 and 0.82 for the $SrIrO_3$ placing the growths in an absorption controlled regime shown to be successful for the growth of other Ruddlesden-Popper systems[1–8]. In situ reflection high-energy electron diffraction (RHEED) was used to monitor the film growth. A representative image shows sharp streaks indicating a smooth surface of $Sr_{1.93}K_{0.07}IrO_4$ (supplementary fig. 1). Fluxes were calibrated using a quartz crystal microbalance (QCM) before growth and by RHEED oscillations during growth of the $SrIrO_3$. Growth of the Sr_2IrO_4 did not display RHEED oscillations, but produced a similar surface quality likely because Sr_2IrO_4 grows in step-flow mode for the growth

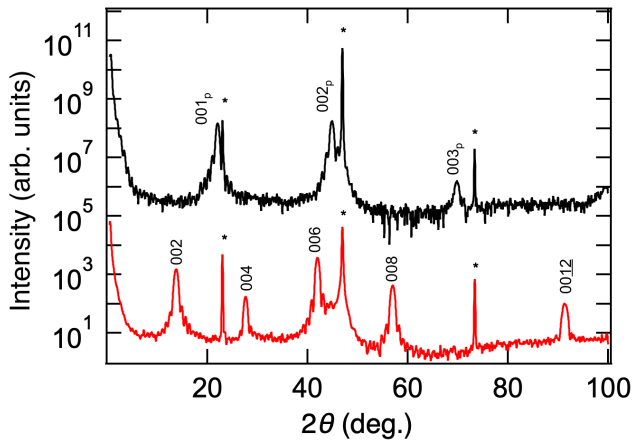

Supplementary Figure 2. X-ray diffraction 2θ scans exhibiting clear thickness fringes from both Sr_2IrO_4 (red) and $SrIrO_3$ (black), peaks due to the $(LaAlO_3)_{0.3}$ $(SrAl_{1/2}Ta_{1/2}O_3)_{0.7}$ (LSAT) substrate are indicated by *.

conditions used.

The structure of the resulting films was characterized through x-ray diffraction with Cu Kα. Supplementary figure 2 shows 2θ scans on representative Sr_2IrO_4 and $SrIrO_3$ samples indicating that both films are phase pure and exhibit thickness fringes, indicating high quality crystalline growth with sharp interfaces.

In total, eleven $Sr_{2-x}K_xIrO_4$ thin films were synthesized for this study. For these eleven samples, the post-growth K substitutional diffusion conditions were varied significantly, including (1) the amount of K deposited on the surface was varied by a factor of 40; (2) the concentration of ozone used in the annealing step (both 10% and 80%); (3) and the amount of time during the vacuum annealing (24 to 40 min) and ozone annealing (20 to 55 min). Despite varying all these conditions, we have found that of the seven samples that yielded high quality ARPES spectra which can be reliably analysed, all seven samples give the same extracted hole doping concentration of 7$\pm$ 2% (from Luttinger volume) and a chemical potential shift of $\Delta\mu$ =-0.4 $\pm$ 0.1 eV. It is possible that a 7% doping may be energetically favoured in the substitutional diffusion process, or that this represents the solubility limit of K in Sr_2IrO_4 .

The chemical content of the film was measured using x-ray photoemission spectroscopy with a Mg k-alpha (hν = 1254 eV) Scienta-Omicron DAR 400 twin-anode X-ray source before and after substitutional diffusion of K on the same sample, shown in Supplementary Fig. 3. This

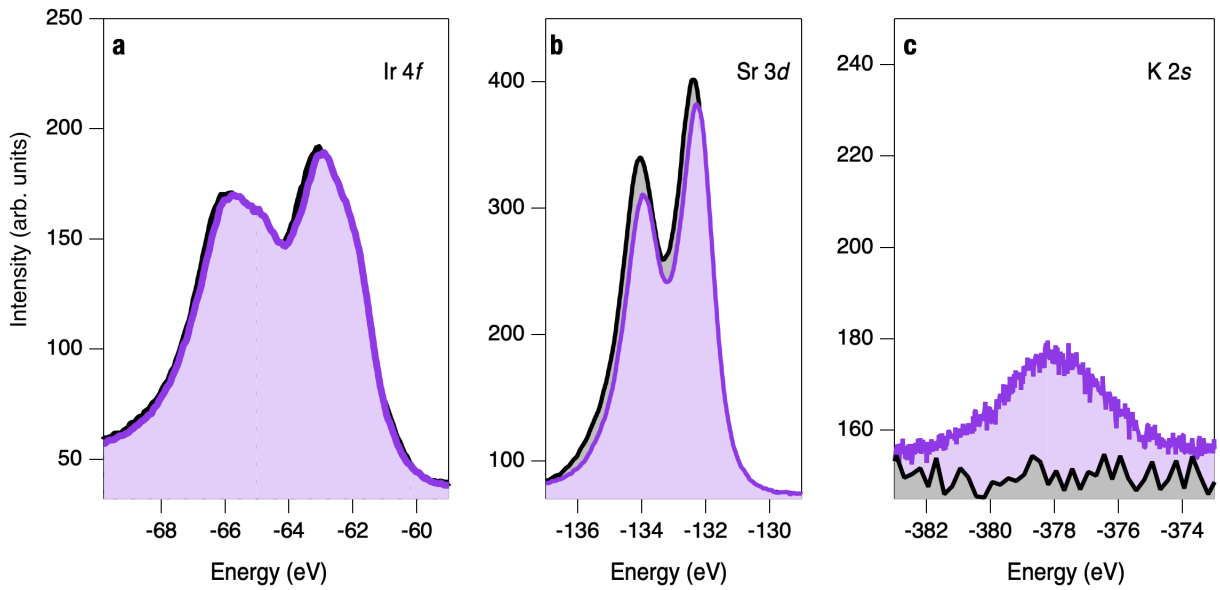

Supplementary Figure 3. Normalized x-ray photoemission spectra of undoped Sr_2IrO_4 (black) and $Sr_{1.93}K_{0.07}IrO_4$ (purple). **a** Ir 4*f* peak, **b** Sr 3*d* peak and **c** K 2*s* peak.

demonstrates that the substitutional diffusion process results in increased K content and decreased Sr content in the region of the sample probed by photoemission. We do not see any signature of the $SrIrO_3$ in photoemission measurements because the thickness of Sr_2IrO_4 is much larger than the inelastic mean free path of electrons with a kinetic energy of 21 eV, 41 eV and 1254 eV[9].

Supplementary Note 2: Control Experiment

In order to confirm that the observed change in electronic structure is due to K dopants and not an unintentional change of oxygen stoichiometry we perform a control experiment where a Sr_2IrO_4 sample is annealed at a temperature of 300 °C in vacuum, followed by exposure to 1×10^{-6} Torr ozone at 300 °C for 20 minutes without first depositing K. Supplementary Figure 4 shows an angle integrated valence band spectra of an as-grown Sr_2IrO_4 sample (black), the same sample after an anneal without K (blue) which shows no change and then after K deposition and the same annealing procedure (red) which significantly alters the spectra and shifts it towards the Fermi level. This demonstrates that K is integral to the process of hole doping.

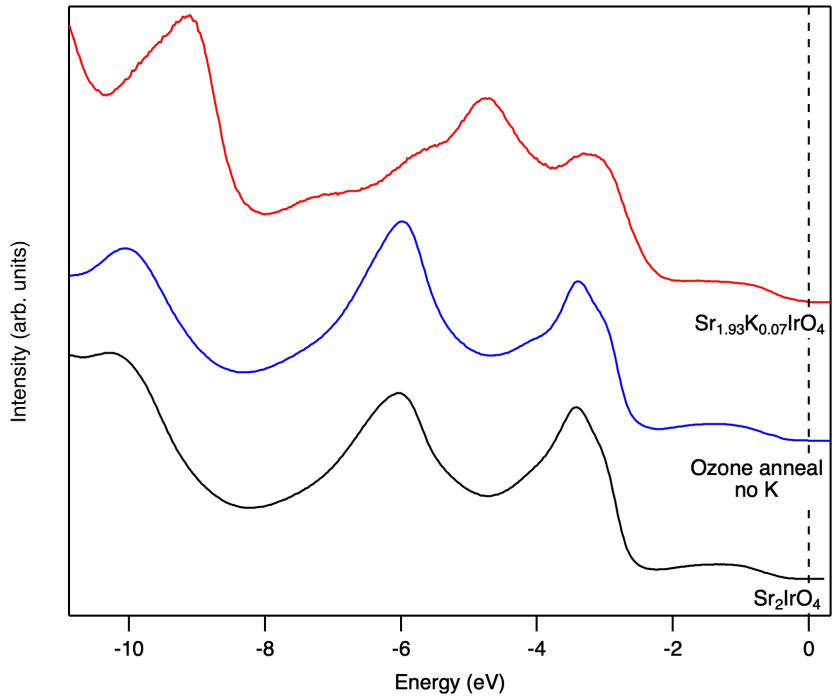

Supplementary Figure 4. Angle-integrated valence band spectra using hν=21.2 eV from an as-grown undoped Sr_2IrO_4 (black), an undoped Sr_2IrO_4 after a 300 °C vacuum then ozone anneal (blue) and a $Sr_{1.93}K_{0.07}IrO_4$ sample that after K deposition was exposed to an identical annealing procedure (red).

Supplementary Note 3: EDC fitting

As discussed in the main text we do not observe a large uniform pseudogap which was reported for $Sr_2Ir_{1-x}Rh_xO_4$ defined by a ∼30 meV leading edge midpoint shift[10,11]. In order to quantify this we fit the energy distribution curves (EDCs) of $Sr_{1.93}K_{0.07}IrO_4$ (Supplementary Fig. 5) to a Fermi-Dirac distribution multiplied by a linear term convoluted by a Gaussian function R_ω, with a full width half max of Δ_E, to account for the energy resolution.

$$f(E) = \left[c + \frac{a + b(E - E_{\mathrm{F}}^{\mathrm{S}})}{1 + e^{(E - E_{\mathrm{F}}^{\mathrm{S}})/k_{\mathrm{B}}T}}\right] * R_\omega, \tag{1}$$

where a is the height of the Fermi step, b is the slope, c is a constant background, E is energy, $E_{\mathrm{F}}^{\mathrm{S}}$ is the leading edge midpoint shift, k_{B} is Boltzmann's constant and T is temperature. The Fermi level $E_{\mathrm{F}}^{\mathrm{Au}}$ was independently verified by measurements of a polycrystalline gold reference in electrical contact with the sample. For all momenta we find a difference between the leading edge midpoint $E_{\mathrm{F}}^{\mathrm{S}}$ and the nominal Fermi level $E_{\mathrm{F}}^{\mathrm{Au}}$ of less than 5 meV, which is within

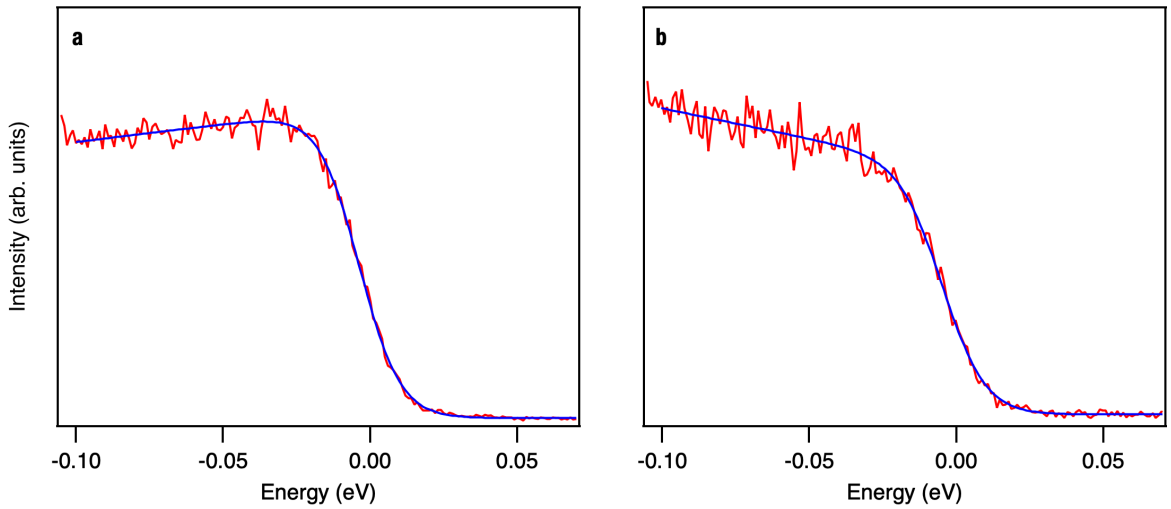

Supplementary Figure 5. Energy distribution curves of $Sr_{1.93}K_{0.07}IrO_4$ reproduced from Fig. 4**e** (red) and fit to Eqn. 1 (blue), fitting parameters are supplied in the main text. **a** EDC at (0, 1.2π). **b** EDC at (π/2,0.6π).

the estimated experimental uncertainty. The fitting parameters used were $\{E_{\rm F}^{\rm S}, a, b, T, c, \Delta_E\}$ = $\{-0.0040 \pm 0.0002\,\mathrm{eV}, 0.526 \pm 0.005, 0.60 \pm 0.07, 72 \pm 2\,\mathrm{K}, 0.009 \pm 0.002, 11\,\mathrm{meV}\}$ at (0, 1.2π) in Supplementary Fig. 5a and $\{-0.0043 \pm 0.0004\,\mathrm{eV},\ 0.301 \pm 0.006, -0.73 \pm 0.08, 77 \pm 4\,\mathrm{K}, 0.011 \pm 0.002, 11\,\mathrm{meV}\}$ at (π/2, 0.6π) in Supplementary Fig. 5b.

Supplementary Note 4: Tight Binding calculation

The tight binding model, described in the main text, has previously been applied to describe both undoped and electron-doped Sr_2IrO_4 and is described in detail in refs[12–14]. We reproduce the relevant details here for convenience of the reader. The Hamiltonian, $H = H_0 + H_{\rm SO} + H_U$ includes

$$H_0 = \begin{pmatrix} \Delta_t + e_1(t_1/t_0)^2 & 0 & 0 & -4\gamma l t_1 & 0 & 0 \\ 0 & 0 & 0 & 0 & -2\gamma l t_2 & 0 \\ 0 & 0 & 0 & 0 & 0 & -2\gamma l t_3 \\ -4\gamma l^\dagger t_1 & 0 & 0 & \Delta_t + e_1(t_1/t_0)^2 & 0 & 0 \\ 0 & -2\gamma l^\dagger t_2 & 0 & 0 & 0 & 0 \\ 0 & 0 & -2\gamma l^\dagger t_3 & 0 & 0 & 0 \end{pmatrix}, \qquad (2)$$

where $t_0 = 0.35$ eV, $\Delta t = 0.15$ eV is the tetragonal crystal field splitting, $\lambda = 0.57$ eV is the SOC parameter, $e_1 = -1.5$ eV, $t_1 = t_0 cos(k_x/2)cos(k_y/2), t_2 = t_0 cos[(k_x + k_y)/2], t_3 = t_0 cos[(k_x - k_y)/2]$ are hopping parameters for the d_{xy}, d_{yz} and d_{zx} orbitals and $l = e^{-i(k_x+k_y)/2}$ describes the reconstruction due to in-plane octahedral rotation, which as shown in Supplementary Fig. 1 also exist in the $Sr_{1.93}K_{0.07}IrO_4$ sample. The basis used is: $\left\{\langle d_{A_{xy}\uparrow}\rangle, \langle d_{A_{yz}\downarrow}\rangle, \langle d_{A_{zx}\downarrow}\rangle, \langle d_{B_{xy}\uparrow}\rangle, \langle d_{B_{yz}\downarrow}\rangle, \langle d_{B_{zx}\downarrow}\rangle\right\}$, which are degenerate to the time-reversed pairs: $\left\{\langle d_{A_{xy}\downarrow}\rangle, \langle d_{A_{yz}\uparrow}\rangle, \langle d_{A_{zx}\uparrow}\rangle, \langle d_{B_{xy}\downarrow}\rangle, \langle d_{B_{yz}\uparrow}\rangle, \langle d_{B_{zx}\uparrow}\rangle\right\}$. γ is a tuning parameter which account for differences between the theory and experiment. We use the same values as ref[14]: $\gamma = 1$ for U= 0 eV and $\gamma = 0.65$ for U = 2 eV. The spin orbit coupling is described by:

$$H_{\mathrm{SO}} = \begin{pmatrix} 0 & \lambda/2 & -i\lambda/2 & 0 & 0 & 0 \\ \lambda/2 & 0 & -i\lambda/2 & 0 & 0 & 0 \\ i\lambda/2 & i\lambda/2 & 0 & 0 & 0 & 0 \\ 0 & 0 & 0 & 0 & \lambda/2 & -i\lambda/2 \\ 0 & 0 & 0 & \lambda/2 & 0 & -i\lambda/2 \\ 0 & 0 & 0 & i\lambda/2 & i\lambda/2 & 0 \end{pmatrix}, \tag{3}$$

and Coulomb repulsion is described by:

$$H_U = \begin{pmatrix} -U\langle n_{A_{xy}\uparrow}\rangle & 0 & 0 & 0 & 0 & 0 \\ 0 & -U\langle n_{A_{yz}\downarrow}\rangle & 0 & 0 & 0 & 0 \\ 0 & 0 & -U\langle n_{A_{zx}\downarrow}\rangle & 0 & 0 & 0 \\ 0 & 0 & 0 & -U\langle n_{B_{xy}\uparrow}\rangle & 0 & 0 \\ 0 & 0 & 0 & 0 & -U\langle n_{B_{yz}\downarrow}\rangle & 0 \\ 0 & 0 & 0 & 0 & 0 & -U\langle n_{B_{zx}\downarrow}\rangle \end{pmatrix}. \tag{4}$$

We solve for $\langle n_{\alpha\sigma}\rangle$ self consistently by numerically diagonalizing the Hamiltonian, calculating the density of states and Fermi level to determine the average occupation for each orbital[15], the on-site energy depends on the occupation of the opposite spin $\langle n_{\alpha\bar{\sigma}}\rangle$, which is equal to $\langle n_{\alpha\sigma}\rangle$ because all bands are doubly degenerate Kramers pairs. For the calculation of undoped Sr_2IrO_4 shown in Fig. 2a and Fig. 4(a-c) $U = 2eV, n_{tot} = 5$, $\left\{\langle n_{A_{xy}\uparrow}\rangle, \langle n_{A_{yz}\downarrow}\rangle, \langle n_{A_{zx}\downarrow}\rangle, \langle n_{B_{xy}\uparrow}\rangle, \langle n_{B_{yz}\downarrow}\rangle, \langle n_{B_{zx}\downarrow}\rangle\right\} = \{0.882, 0.614, 0.614, 0.981, 0.954, 0.954\}$.

Supplementary References

* kmshen@cornell.edu

[1] Shai, D. E. *et al.* Quasiparticle mass enhancement and temperature dependence of the electronic structure of ferromagnetic $SrRuO_3$ thin films. *Phys. Rev. Lett.* **110**, 087004 (2013).

[2] Uchida, M. *et al.* Correlated vs. conventional insulating behavior in the $j_{\mathrm{eff}} = \frac{1}{2}$ vs. $\frac{3}{2}$ bands in the layered iridate Ba_2IrO_4. *Phys. Rev. B* **90**, 075142 (2014).

[3] Nie, Y. F. *et al.* Interplay of spin-orbit interactions, dimensionality, and octahedral rotations in semimetallic $SrIrO_3$. *Phys. Rev. Lett.* **114**, 016401 (2015).

[4] Burganov, B. *et al.* Strain control of fermiology and many-body interactions in two-dimensional ruthenates. *Phys. Rev. Lett.* **116**, 197003 (2016).

[5] Kawasaki, J. K., Uchida, M., Paik, H., Schlom, D. G. & Shen, K. M. Evolution of electronic correlations across the rutile, perovskite, and ruddelsden-popper iridates with octahedral connectivity. *Phys. Rev. B* **94**, 121104 (2016).

[6] Nair, H. P. *et al.* Demystifying the growth of superconducting Sr_2RuO_4 thin films. *APL Materials* **6**, 101108 (2018).

[7] Nair, H. P. *et al.* Synthesis science of $SrRuO_3$ and $CaRuO_3$ epitaxial films with high residual resistivity ratios. *APL Materials* **6**, 046101 (2018).

[8] Liu, Y., Nair, H. P., Ruf, J. P., Schlom, D. G. & Shen, K. M. Revealing the hidden heavy fermi liquid in $CaRuO_3$. *Phys. Rev. B* **98**, 041110 (2018).

[9] Seah, M. P. & Dench, W. A. Quantitative electron spectroscopy of surfaces: a standard data base for electron inelastic mean free paths in solids. *Surf. Interface Anal* **1**, 2–11 (1979).

[10] Louat, A. *et al.* Formation of an incoherent metallic state in Rh-doped Sr_2IrO_4. *Phys. Rev. B* **97**, 161109 (2018).

[11] Louat, A. *et al.* ARPES study of orbital character, symmetry breaking, and pseudogaps in doped and pure Sr_2IrO_4. *Phys. Rev. B* **100**, 205135 (2019).

[12] Jin, H., Jeong, H., Ozaki, T. & Yu, J. Anisotropic exchange interactions of spin-orbit-integrated states in Sr_2IrO_4. *Phys. Rev. B* **80**, 075112 (2009).

[13] Carter, J.-M., Shankar V., V. & Kee, H.-Y. Theory of metal-insulator transition in the family of perovskite iridium oxides. *Phys. Rev. B* **88**, 035111 (2013).

[14] De La Torre, A. *et al.* Collapse of the Mott gap and emergence of a nodal liquid in lightly doped

Sr_2IrO_4. *Phys. Rev. Lett.* **115**, 176402 (2015).

[15] Claveau, Y., Arnaud, B. & Matteo, S. D. Mean-field solution of the Hubbard model: the magnetic phase diagram. *Eur. J. Phys.* **35**, 035023 (2014).